Solar Physics (2005) 226: 283–315
DOI: 10.1007/s11207-005-7417-9

THE NOAA GOES-12 SOLAR X-RAY IMAGER (SXI) 2. PERFORMANCE

V. J. PIZZO[1], S. M. HILL[1], C. C. BALCH[1], D. A. BIESECKER[1], P. BORNMANN[1,*], E. HILDNER[1], R. N. GRUBB[1], E. G. CHIPMAN[2], J. M. DAVIS[3], K. S. WALLACE[3], K. RUSSELL[3], S. A. CAUFFMAN[4], T. T. SAHA[4] and G. D. BERTHIUME[5]

[1]*NOAA Space Environment Center, 325 Broadway, Boulder, CO 80305, U.S.A.*
[2]*NOAA NESDIS/SOCC, Suitland, MD 20746, U.S.A.*
[3]*NASA Marshall Space Flight Center, Huntsville, AL 35812, U.S.A.*
[4]*NASA Goddard Space Flight Center, Greenbelt, MD 20771, U.S.A.*
[5]*MIT Lincoln Laboratories, Lexington, MA 02420, U.S.A.*
[*]*Present address: Ball Aerospace & Technologies Corp., 1600 Commerce Street, Boulder, CO 80306-1062, U.S.A.*
(e-mail: vic.pizzo@noaa.gov)

(Received 27 August 2004; accepted 29 November 2004)

Abstract. The Solar X-ray Imager (SXI) was launched on 23 July 2001 on NOAA's GOES-12 satellite and completed post-launch testing on 20 December 2001. It was brought into operations on 21 January 2003. This paper documents SXI performance and calibrations prior to an instrument degradation that occurred on 5 November 2003 and thus covers more than 420 000 soft X-ray images of the Sun. This paper details component-level as well as full-system calibrations characterizing the spatial and spectral performance of the instrument, including the grazing-incidence mirror, filters, and the properties of the MCP-intensified CCD detector system. Routine image corrections are also described. These include background (dark current) subtraction, flat-fielding, off-band light-leak correction, and image pointing and timing considerations. In addition, a signal-to-noise analysis is presented. The information contained in this study is intended to enable researchers to conduct quantitative analysis of GOES-12 SXI images.

1. Introduction

NOAA's GOES-12 Solar X-ray Imager (SXI), which was built by NASA's Marshall Space Flight Center (MSFC) with funding from the US Air Force, was launched on 23 July 2001. The physical design and operations of the instrument are detailed elsewhere (Hill *et al.*, 2005; hereafter, Paper 1). This document addresses the performance and calibration of the flight optics to provide the basis for quantitative analysis of the solar image data collected by GOES-12 SXI. The characterization presented here applies mainly to observations taken prior to 5 November 2003, since which time hardware degradations suffered by the instrument have imposed limitations upon its operation and altered its spectral response in ways that have yet to be fully quantified.

This paper opens with a brief recap of the GOES-12 SXI hardware and spacecraft accommodation, followed by a statement of performance goals. Succeeding

sections address the spatial and spectral response of the optical components and full system, relevant image corrections, and the signal-to-noise properties of the system.

2. Instrument Description

A complete description of the GOES-12 SXI instrument is presented in Paper 1, so only a brief sketch is included here.

SXI images the Sun with a nominal 1-min cadence in the 0.6–8.0 nm range, at 5 arcsec spatial resolution. The instrument uses a classic Wolter I grazing-incidence optical design with a nickel-coated, monolithic Zerodur mirror. Metallic thin-film entrance filters arranged in six annular segments about the front of the instrument reject IR-visible-UV solar radiation. A set of selectable thin film filters near the focal plane allows for rudimentary plasma temperature discrimination. The detector is comprised of three components: a microchannel plate (MCP) intensifier, a fiber optic taper (FOT), and a visible-light charge-coupled device (CCD). The MCP acts like an array of photomultiplier tubes whose gain depends upon an applied voltage. The resulting electron clouds impact a phosphor plate that emits at visible wavelengths. The phosphor is optically linked via the FOT to a 512×512 pixel CCD. An ultraviolet illumination source (UV lamp) is included for detector aliveness verification.

This complex detection system has many benefits. The MCP blocks visible light, and this requires less attenuation of visible light by filters which also attenuate low energy soft X-rays of interest. In combination with the photon counting nature of the detector, substantial improvements in sensitivity to emissions from plasmas below 2 MK are achieved when compared to bare CCDs available at the time of construction. The detector configuration allows for adjustable gain that can be used in conjunction with exposure time to control signal to noise and dynamic range. The design also provides electronic shuttering by controlling the accelerating voltage across the MCP. This voltage is turned on and off with rise times of 100 μs to accommodate exposure times as short as 1.5 ms.

The SXI is mounted on the yoke of the GOES-12 solar array drive assembly (SADA), which is stepped in azimuth every 3.33 s to keep the Sun in the field of view as the spacecraft orbits about Earth (Zimmermann, Zwirn, and Davis, 2004). Operational control of imaging sequences is driven by a set of on-board tables that can be modified by ground command. A High-Accuracy Sun Sensor (HASS) integrated into the instrument provides pointing knowledge.

SXI underwent extensive optical testing at both the component and full instrument level prior to launch. The first set of tests were conducted at the MSFC Stray Light Facility (SLF) in January-February 1997 and a second set at the X-ray Calibration Facility (XRCF) in February 1998. The XRCF tests were undertaken to resolve issues regarding lower than anticipated sensitivity of the instrument at 8.33 Å, as indicated by SLF testing. Also, they provided an opportunity to repeat and to expand upon the SLF performance tests. The results of the XRCF measurements

TABLE I
Instrument performance specifications.

	Test source	Minimum detectable flux ($erg\,cm^{-2}\,arcsec^{-2}\,s^{-1}$)
Spectral sensitivity	Al (8.3 Å)	1.5×10^{-8}
	C (44.7 Å)	6.0×10^{-8}
Spatial resolution		Ensquared energy (pix × pix)
On-axis	C (44.7 Å)	1 × 1, 25% (40% goal)
		2 × 2, 40% (60% goal)
Off-axis (15 arcmin)	Al (8.3 Å)	Rayleigh-like splitting of 2 point-sources 15 arcsec apart

are the primary basis for ground-based operational calibrations of SXI. Additional calibrations were also performed on orbit during post-launch testing (PLT) from September to December 2001 and upon SXI reactivation in January 2003. The results of the ground testing as well as relevant in-orbit testing are presented in the following sections. Full-instrument and component performance evaluations are included as appropriate.

3. Performance Requirements

In view of its mission of detecting large-scale solar activity likely to impact the geospace environment, the spatial resolution and spectral sensitivity requirements for SXI are modest, relative to cutting-edge research instrumentation. The key performance requirements are summarized in Table I.

These requirements were designed to ensure adequate sensitivity for important solar features within the 3-s maximum operational exposure interval and to provide a spatial resolution of about 10 arcsec (or better) over most of the solar image. In the table, the point-spread requirement is stated in terms of ensquared energy, the percentage of the total energy in a point-source image falling within an $n \times n$ pixel area of the detector. Design goals are presented in parentheses.

4. Spatial Performance

4.1. On-axis image properties

The XRCF provides a stable x-ray point source about 0.2 arcsec in angular diameter. The beam is uniform across the instrument aperture and photon fluxes associated with the various sources [Al (8.33 Å), Mg (9.89 Å), Cu (13.3 Å), and C (44.7 Å)] are well calibrated. During testing the instrument was maintained in a vacuum of

$\sim 10^{-6}$ torr and its temperature was regulated. Fluxes at the XRCF are more than an order of magnitude lower than typical non-flare values, so some exposures for the point-source tests had to be as long as the SXI camera hardware limit of 65 s.

The radiation from the point source spreads out in the instrument due to the combined optical action of the mirror and the detector. As will be detailed below, the width and shape of the image core is largely determined by spreading in the detector, whereas the near wings of the distribution result from the figure of the SXI mirror. In addition, the detector contributes another diffuse spreading component at large distances from the image core.

A series of 8.33 Å and 44.7 Å point-source images was taken to establish system on- and off-axis point-spread function (PSF) properties. Due to the low source fluxes, the MCP was run at 873 V to obtain well-exposed image cores. This is well above typical operating voltages of 550–750 V, so certain aspects of the ground test calibrations have to be supplemented by on-orbit measurements. (See Section 5.2.) The collected images were screened for defects, and a reference dark-current background image was subtracted from each. The point images within a set were individually centroided and referenced to a common center for compositing, and radially binned averages of the composited data were taken.

The mean profiles for point images lying on the optical axis are shown in Figure 1 (left). Out to roughly 80 arcsec the profile approximates a Moffat function (Martens, Acton, and Lemen, 1995):

$$M(r) = \frac{A}{[1 + (r/r_0)^2]^B}, \tag{1}$$

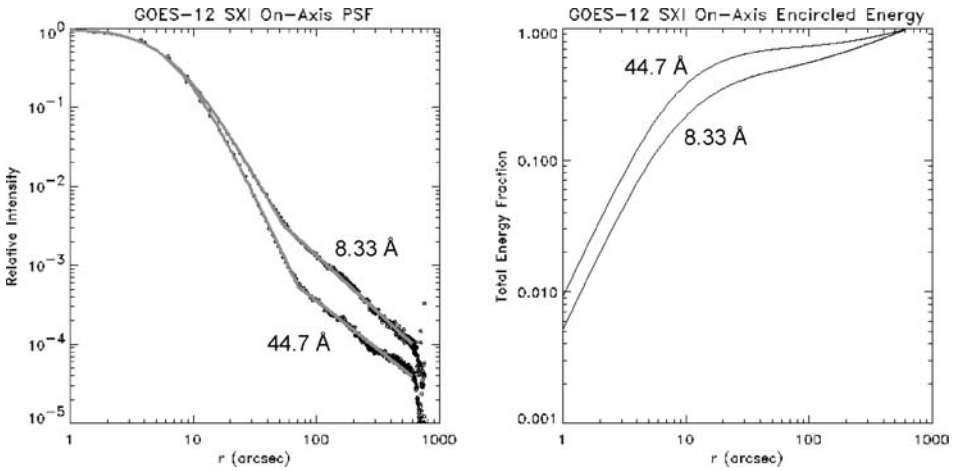

Figure 1. Radial intensity profile (*left*) of composited 8.33 Å and 44.7 Å on-axis point-source test images; *right*: encircled energies.

whereupon a power law decline

$$P(r) = \frac{P_0}{[1 + r]^D} \tag{2}$$

extends out to about 700 arcsec. This outer portion of the profile has been dubbed "the halo". The parameters A, B, r_0, P_0, and D, as defined in Equations (1) – (2), are empirically determined from the test image data (see Tables II–IV for numerical values).

As referenced above, the Moffat function profile had been used to model the Yohkoh SXT PSF. The extended power-law component, however, was an unforeseen consequence of the detector design. The halo was first detected in the SXI PSF test composites, as its low amplitude rendered it virtually invisible in individual test images, except in unusually deep, specially processed exposures (e.g., see Figure 2, left). In operations, however, it can be spectacularly visible in flare images, as exemplified in Figure 2, right. The halo evidently originates in the interface between the bottom of the MCP and the phosphor, where secondary photoelectrons undergo wide-angle scattering that has a sharp cutoff beyond a certain cone angle (Ientilucci, 2000). Additional lateral spreading may also occur in the FOT. The net effect is a pervasive fogging of the image, although it is most prominent about bright

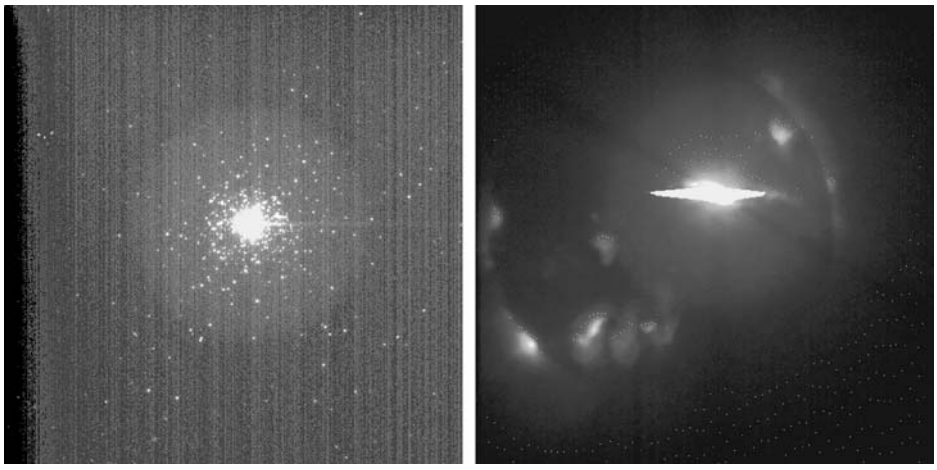

Figure 2. Left: composite of two 64-s 907 V exposures taken at 44.7 Å during XRCF testing. The image has been scaled to bring out faint details, so the bright core of the point-source is saturated. The halo is the diffuse glow extending to large distances about the core; it originates in the detector as described in the text. The dots peppering the CCD face and clustering around the core are individual photons wide-angle scattered by the mirror. The dark feature along the left edge is an artifact of the test setup. *Right*: 700 V 3-s patrol exposure taken with the thin Be filter on 4 November 2001 during an X-class flare associated with an erupting sigmoid, showing the halo, CCD blooming, and six subtle dark channels emanating from the bright source center. The latter are most likely due to the supports for the entrance filter, which is mounted in six separate annular segments.

sources. This behavior has been encountered in military night-vision devices (e.g., Estrera *et al.*, 2003). Characteristically, the SXI halo does not appear to be a function of field angle, MCP voltage, or wavelength, although the latter two properties are hard to pin down in ground-based test data because of the low fluxes. Patrol observations of bright solar flares provide an opportunity to refine these properties further (e.g., see Gburek and Sylwester, 1999).

An approximation to the measured SXI on-axis PSF is given by the piece-wise continuous function

$$F(r) = \left\{ \begin{array}{l} M(r) \\ P(r) \\ C(r) \end{array} \right\} \left\{ \begin{array}{l} 0 < r < R_{p1} \\ R_{p1} < r < R_{p2} \\ r > R_{p2} \end{array} \right. , \tag{3}$$

where

$$R_{p1} = \left(\frac{A}{P_0} r_0^{2B} \right)^{[1/(2B-D)]} \tag{4}$$

is the distance to the inner edge of the power-law region and $R_{p2} = 700$ arcsec marks the relatively sharp outer edge of the halo. The steep cutoff beyond R_{p2}, which is modeled by the function $C(r)$, is real; it is associated with the halo phenomenon and is not an artifact of low signal strength at large r. Because of the low ground test fluxes, $C(r)$ is poorly determined, but a suitably smooth approximation that supports PSF deconvolution is

$$C(r) = P(R_{p2}) \exp\left(-(r - R_{p2})/\kappa\right), \tag{5}$$

where κ is of the order of 30 arcsec.

The corresponding on-axis encircled energy measures are plotted in Figure 1 (right). The encircled energy values in the core should be multiplied by a factor of $4/\pi$ for comparison against the ensquared energy criteria in the design specifications. The instrument falls short of the on-axis targets in Table I. For example, at the 44.7 Å test wavelength the measured 1×1 pixel energy is about 8%, and the 2×2 pixel value is just 23%. In addition, the net energy scattered into the halo region is substantial, being of the order of 1/3 of all the energy in the electron cloud generated by the MCP.

It is to be emphasized that ground testing indicates the full width at half maximum (FWHM) spreading in the mirror itself is of the order of 2 arcsec. Thus the bulk of the spreading in the SXI PSF core arises in the detector. There is measurable wide-angle scattering associated with greater-than-expected microroughness, but this is at a level well below that of the halo. Finally, it is important to be aware that the PSF figures herein refer to the flight focus, which was intentionally offset (de-focused) by some 60 μ to flatten the overall focus over a wider field of view than is normally obtained with Wolter I optics.

4.2. OFF-AXIS IMAGE PROPERTIES

The off-axis properties were tested by off-pointing the SXI instrument so that the XRCF point-image fell upon the CCD face at a progression of locations away from the optical axis. Axially averaged values for the fit parameters A, r_0, B, P_0, and D at various field angles are given in Tables II and III for both discrete test wavelengths. The FWHM in the core of the PSF,

$$\mathrm{FWHM} = 2r_0\sqrt{2^{1/B} - 1}, \tag{6}$$

is included as a useful gauge of the spatial resolution.

The shape of the Moffat core of the PSF as a function of field angle has also been determined from the 870 V data. Figure 3 presents a series of contour maps of the FWHM at both 8.33 Å and 44.7 Å wavelengths. Each panel depicts the mean FWHM at a particular field angle (angular distance from the optical axis) broken down into contributions from 8 separate sectors about the point-image core, with the sector at the 9 o'clock position lying nearest the instrument optical axis. Field angle increases from left to right. The progression from a relatively tight, circular cross-section to a broader, distorted shape is evident. Figure 3 shows a reasonably uniform focus within the region of a properly centered solar disk, which confirms the efficacy of the intentional flight defocus. The maximum asymmetry in the core,

TABLE II
Fit parameters at 873 V, 8.33 Å.

Fld angle (arcmin)	A (rel. ampl)	r_0 (arcsec)	B	P_0 (rel. ampl)	D	FWHM (arcsec)
2	1.00 ± .013	6.43 ± 0.12	1.34 ± 0.01	1.04 ± 0.22	1.44 ± 0.04	10.6 ± 0.24
8	0.937 ± .012	6.83 ± 0.12	1.37 ± 0.02	0.88 ± 0.18	1.42 ± 0.04	11.1 ± 0.24
12	0.679 ± .018	7.88 ± 0.16	1.40 ± 0.02	1.22 ± 0.28	1.50 ± 0.04	12.6 ± 0.33
16	0.432 ± .007	11.1 ± 0.24	1.61 ± 0.03	1.01 ± 0.25	1.48 ± 0.05	16.3 ± 0.45
20	0.243 ± .004	15.8 ± 0.44	1.82 ± 0.04	0.73 ± 0.17	1.43 ± 0.05	21.6 ± 0.81

TABLE III
Fit parameters at 873V, 44.7 Å.

Fld angle (arcmin)	A (rel. ampl)	r_0 (arcsec)	B	P_0 (rel. ampl)	D	FWHM (arcsec)
2	1.00 ± .009	7.26 ± 0.08	1.65 ± 0.01	0.107 ± .032	1.24 ± 0.06	10.5 ± 0.15
8	0.979 ± .008	7.52 ± 0.08	1.66 ± 0.01	0.076 ± .019	1.16 ± 0.05	10.8 ± 0.14
12	0.751 ± .006	8.74 ± 0.09	1.74 ± 0.01	0.057 ± .013	1.11 ± 0.04	12.3 ± 0.12
16	0.476 ± .004	12.3 ± 0.14	1.99 ± 0.02	0.067 ± .013	1.15 ± 0.04	15.8 ± 0.23
20	0.330 ± .003	16.4 ± 0.21	2.28 ± 0.03	0.057 ± .006	1.12 ± 0.01	19.6 ± 0.33

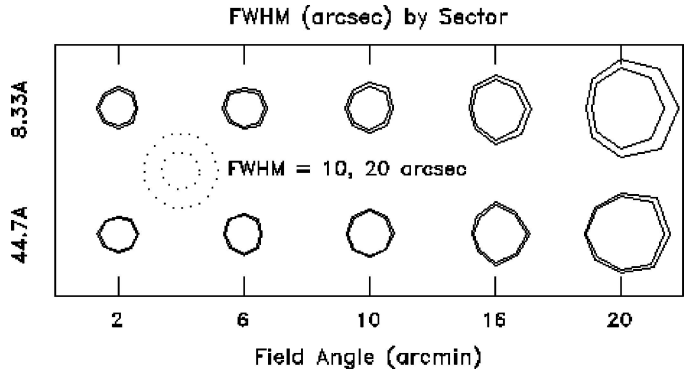

Figure 3. Moffat FWHM core shape as function of field angle, at 8.33 Å (upper) and 44.7 Å (lower). Optical axis is to the left (field angle = 0). Patterns are taken to be symmetric about the optical axis. The two contour levels are indicative of the dispersion in the FWHM estimates for each sector.

as measured by directional variations in the FWHM, ranges from about 5% on axis to 12% at 20 arcmin. It is to be noted that the much broader halo contribution exhibits no systematic distortion of shape with field angle.

4.3. MCP VOLTAGE DEPENDENCE

SXI image properties depend heavily upon the MCP voltage since it determines the number of electrons elicited by each detected photon. At high voltages (750 – 1000 V), fewer photons are needed to achieve saturation in the CCD, and images take on a more granular appearance; at low voltages (500 – 700 V), many more photons contribute to the image, which has a smoother look. In principle, the smaller electron clouds at lower voltages allow for a sharper image.

To support analysis of this effect, a series of on-axis point-source images was taken over a range of MCP voltages (873 V, 828 V, 747 V, and 699 V) at 44.7 Å. At these lower voltages, the signal per photon collected in the detector drops sharply (see Section 5.2), so as many as 180 images were gathered at each voltage setting to assure statistical integrity.

The dependence of the on-axis image fit parameters and FWHM as a function of MCP voltage at 44.7 Å is shown in Table IV. The lowest voltage at which testing could be conducted is at the upper end of the operational range; thus, the typical FWHM for most SXI patrol images should be somewhat better than the 9 arcsec value listed for 699 V.

Two additional issues merit comment. First, the SXI spatial resolution varies slightly over the course of the year due to thermal variations associated with changing spacecraft attitude with respect to the Sun. Operational experience suggests the magnitude of the variation is negligible, relative to other contributions to the net PSF. The second issue, not yet analyzed, is the effect upon the PSF of charge pile-up

TABLE IV
Fit parameters over range of voltage, 44.7 Å.

MCP (volts)	A (rel. ampl)	r_0 (arcsec)	B	P_0 (rel. ampl)	D	FWHM (arcsec)
699	$1.00 \pm .003$	5.94 ± 0.03	1.54 ± 0.01	$0.093 \pm .037$	1.29 ± 0.08	8.96 ± 0.06
747	$1.00 \pm .004$	6.20 ± 0.03	1.59 ± 0.01	$0.129 \pm .032$	1.40 ± 0.05	9.16 ± 0.05
828	$1.00 \pm .015$	6.11 ± 0.09	1.53 ± 0.01	$0.043 \pm .012$	1.09 ± 0.06	9.26 ± 0.16
873	$1.00 \pm .009$	7.26 ± 0.08	1.65 ± 0.01	$0.107 \pm .031$	1.24 ± 0.06	10.5 ± 0.14

arising from nonlinear response of the MCP under conditions of high photon flux (see Section 5.2).

Finally, it is crucial to re-emphasize that the results presented here do not represent operational exposure times and MCP voltage settings for the SXI. Modeling the operational SXI PSF requires careful extrapolation of the ground test data.

4.4. The effects of pointing accuracy and jitter

The rotation of the GOES spacecraft solar panels (SADA) to track the Sun has the potential to generate motions that would seriously degrade SXI imaging properties. It was predicted that a predominantly east-west oscillation of the order of 15 arcsec could be expected if GOES-12 were to be operated in the conventional single-step SADA tracking mode (one SADA step every 1.67 s). Engineering simulations showed that a staggered double step – with a suitable phase shift between the two steps – would reduce these vibrations to an acceptable level. The SADA electronics were therefore redesigned to allow for a programmable time delay between steps to damp oscillations at the dominant disturbance frequencies. Provision was made in the PLT test schedule to obtain sufficient HASS data to assess the resultant motions over a range of SADA double-step phasing (see also Sudey, 2002a, b).

Figure 4 (left) shows the resultant spacecraft pointing motions for the optimized operational phasing of 280 ms. The plot of the east–west (EW) motions includes two successive SADA double step intervals, which occur every $\sim$3.3 s. The intra-step 15 arcsec per sec (3 pixel/s) drift is subtracted out smoothly from the EW curve to highlight the character of the residual spacecraft vibrations. The associated north–south (NS) motions are also depicted. It can be seen that the double stepping effectively suppresses the EW motions throughout the inter-step "quiet" period and that the more regular, initially larger NS motions damp out near the middle of this period. The imaging strategy is to take exposures as far as possible toward the end of each quiet period. The long 3-s patrol images must necessarily compromise some spatial resolution due to jitter to gain the sensitivity to detect faint features.

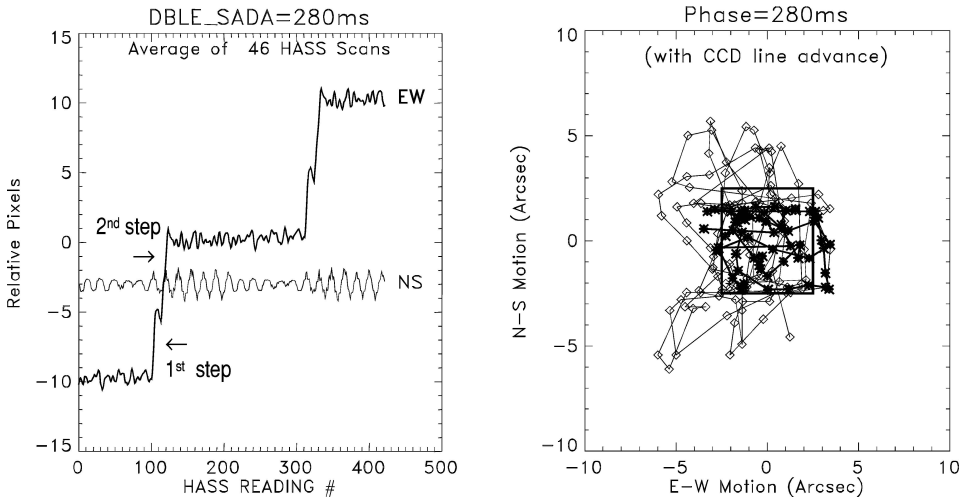

Figure 4. Observed GOES-12 spacecraft motions associated with the tracking of the solar array. Plot *at left* shows east–west and north–south motions across two SADA double steps, as measured in HASS reading intervals of 0.016 s. *At right* is a hodograph of the image motions during the ∼3 s quiet period between the double steps, including the effects of CCD line advance. The final 1-s portion of the 3-s quiet interval is highlighted by asterisks connected by the *heavy line*. Box at plot center indicates pixel size.

In operation, the inter-step EW drift is compensated for by advancing the columns of the CCD every third of a second (see Paper 1, Section 3.2). The line advance imposes an effective saw-tooth EW motion with a period of 0.333 s, a peak-to-trough amplitude of 5 arcsec, and an RMS of 1.4 arcsec about the mean. For 280 msec double-step phasing, the residual EW motions in a 3-s exposure are about 1.75 arcsec RMS. Thus, when the mean EW motion is convolved with the CCD line advance and the NS motions (2.3 arcsec RMS), the net image RMS due to spacecraft jitter is about 3.2 arcsec. Thus, the jitter contributes only minimally to the overall PSF, which is dominated by the optical and detector responses.

5. Spectral Response and System Throughput

The responses of the SXI optical components were measured individually during instrument development, and the throughput of the SXI system as a whole was calibrated twice by ground test at MSFC. The elements affecting the SXI throughput include the mirror, the detector, the prefilter (or entrance filter), and the analysis filters. Each is described in turn in the sections below. In addition, near the entrance filter assembly SXI has an aperture plate, which is designed to improve image sharpness by restricting the bundle of rays passing through to the focal plane. The aperture plate reduces the net throughput by approximately 10% at all wavelengths.

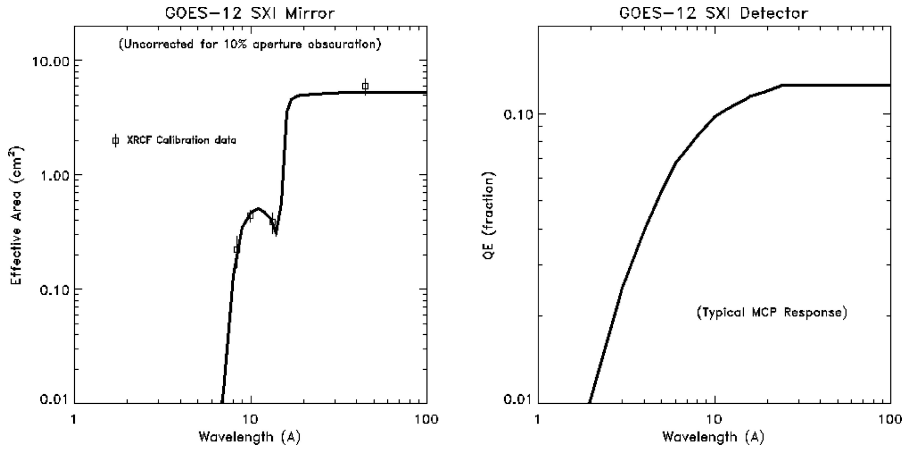

Figure 5. Left: measured SXI mirror effective area. Throughput is reduced by 10% as indicated due to the presence of the aperture plate. *Right*: the SXI MCP detector quantum efficiency.

5.1. MIRROR

Combining physically based models of the mirror reflectivity with calibrated component and system throughput measurements at four discrete wavelengths, the effective area of the mirror as a function of wavelength (Figure 5, left) has been accurately determined (Berthiaume, 1998). The effective area at the shortest wavelengths ($<$15 Å) falls below design expectations (based upon ray-trace simulations) by a factor of 2–3, presumably due to excessive residual microroughness on the mirror surface. The operational consequence is that the hottest coronal material is less visible than anticipated, and images taken with the polyimide and beryllium filters must be run at higher MCP voltages, with concomitant loss of dynamic range (see Appendix).

5.2. DETECTOR: INTEGRATED AND SINGLE-PHOTON RESPONSE

The X-ray photon detecting element in the SXI instrument is an MCP, which directs a cascade of electrons onto a phosphor-coated layer. There the electrons excite visible-light photons that illuminate a CCD through a fiber optic taper that adjusts the plate scale.

At a given MCP voltage, the magnitude of electron cascades triggered within the MCP by individual photon hits is exponentially distributed. The steepness of the distribution – and hence the mean response per photon detected – is strongly dependent upon the MCP voltage. However, the distribution is rigorously independent of incident photon wavelength. Thus the SXI detector is truly a photon-counting device, in that the response of the detector is the same for any *detected* photon, regardless of wavelength. On the other hand, the probability that a photon will trigger a cascade at all – i.e., be detected – does depend upon wavelength, as shown in

Figure 5 (right). This dependence must be convolved with the mirror effective area as a function of wavelength to determine the net spectral response of the instrument.

For routine solar observations the SXI detector functions in photon-integration mode. That is, the detector is exposed for some period, at which time the total charge collected in each pixel of the CCD is read out. (The charge is discretized in units of data number – DN – ranging 0–1023.) Solar features in an SXI image thus represent the superposition of many photon hits. Therefore the calibration of the detector response against an accumulation of overlapping photon hits is a critical step in determining the overall sensitivity of the instrument.

The determination of the absolute response of the SXI detector system, i.e., the $\mathrm{DN/photon_{detected}}$ as a function of MCP voltage (V_{MCP}), is based upon extensive analysis of a combination of laboratory and on-orbit data.

A direct measurement of the detector integrated response was conducted at MSFC (Russell *et al.*, 1996). The detector was exposed to monochromatic X-ray sources of known intensity, and background-subtracted averages of the normalized count rates were then fit as a function of the MCP voltage. Although the response of the MCP itself was anticipated to be essentially exponential, the gain of the combined MCP-phosphor-CCD detector stack was found to be better approximated by a power law than an exponential over the range of MCP voltages where suitable exposures could be obtained with the relatively weak ground-test sources. Figure 6

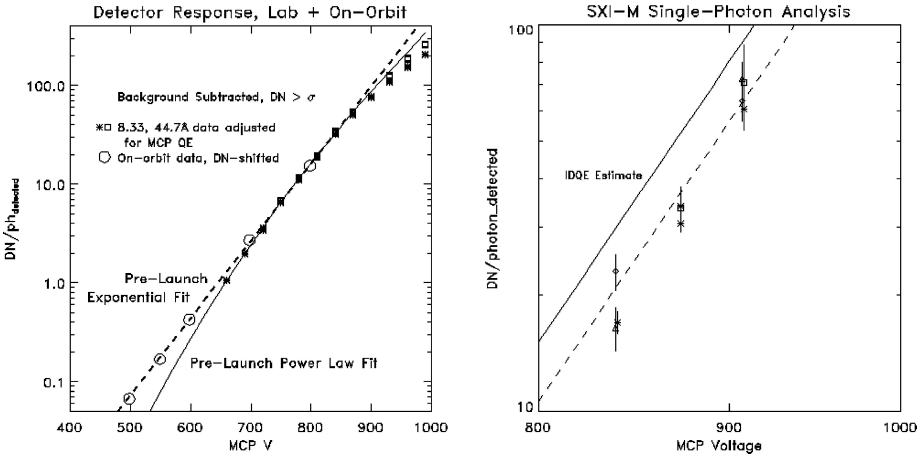

Figure 6. Left: detector response as a function of MCP voltage. Laboratory data for the integrated DN per photon detected is shown at two wavelengths, 8.33 Å (asterisks) and 44.7 Å (squares) wavelengths; these two data sets have been adjusted to account for the differing MCP quantum efficiencies (8% and 12%, respectively; see Figure 5, right). The ratio between the DN per incident photon values in the raw data at the two wavelengths is ∼3/2, consistent with the expected relative quantum efficiencies. On-orbit data based upon solar image analysis (see text) are depicted by *open circles*. Two fits are shown, a power law (*solid*) that better represents the higher-voltage laboratory data and an exponential (*dashed*) that is more appropriate at lower operational voltages. *Right*: power law representation of single-photon and integrated photon calibrations.

(left) shows the power law fit to the data as a solid line. The dashed line shows an alternate exponential fit to the laboratory data, adjusted for the MCP quantum efficiency as specified in the Figure caption.

The observed rollover in response above 850 V in Figure 6 (left) is consistent with detailed simulations of the cascade process in MCPs showing a modest nonlinearity of response with increasing voltage (e.g., Guest, 1971). It is probably not indicative of photon flux saturation. That is, for any MCP there is a finite delay for the electron population in any channel of the MCP to recover from a previous activation. When the incoming photon flux rate exceeds this limit, the response is much reduced. The available test apparatus did not permit direct measurement of the critical saturation rate, but estimates based upon typical MCP properties suggest the channel refresh period to be about 0.5 ms, for moderate voltages. This is about the rate (2000 pulse activations per second per channel) anticipated with the SXI instrument for a typical M-class flare, and it is vastly above the peak ground-test photon rate of <1 photon/s/channel.

Since the operational MCP voltages fall significantly below the range of voltages sampled in the detector response laboratory tests, a special sequence of images was taken during PLT to establish the relative variation of the response as a function of V_{MCP}. With a given filter in place, a rapid series of solar exposures was made at MCP settings between 500 –800 V. Background-corrected whole-image means (adjusted for differences in exposure time) were taken for each set. These data provide a measure of DN/s as a function of V_{MCP} at a relatively fixed – but unknown – photon flux. In Figure 6 (left), we have scaled (shifted vertically) the raw on-orbit data by an arbitrary amount to test the correspondence of these data with the laboratory fits. It is evident that the on-orbit data provide an excellent match to the laboratory exponential fit extended down toward the operational voltage range.

Single photon measures of detector performance were undertaken to obtain corroborative information about the detector response. In particular, the raw laboratory determination of the response was in terms of DN per photon *incident* upon the MCP face. That quantity is related to the DN per photon *detected* (which is needed to estimate the intensity of solar features observed by SXI) via the MCP quantum efficiency (Figure 5, right) as

$$\frac{\mathrm{DN}}{\mathrm{phot}_{\mathrm{detected}}} = \frac{\mathrm{DN}}{\mathrm{phot}_{\mathrm{incident}}} \times \frac{\mathrm{phot}_{\mathrm{incident}}}{\mathrm{phot}_{\mathrm{detected}}}. \tag{7}$$

The last term on the right is just the inverse of the quantum efficiency. Given that the quantum efficiency of the flight MCP was not measured directly (Figure 5, right, is an approximation), it is imperative to verify the above relation by some direct means.

Single-photon pulse-height analysis provides the crucial confirmation. The probability of producing n counts in the detector when the MCP is activated by a single incident photon is

$$P_1(n) = m\ \exp(-mn), \tag{8}$$

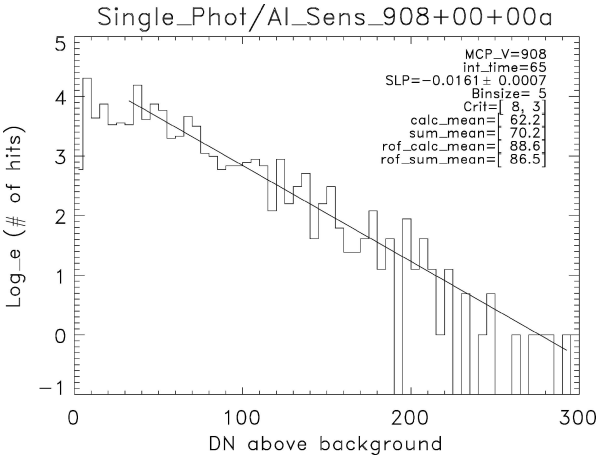

Figure 7. Single-photon statistics for the SXI MCP detector. The mean DN per photon hit is equal to the inverse of the slope of the distribution, m.

where the factor m is determined empirically. In a collection of fixed-voltage images where isolated (non-overlapping) photon hits can be distinguished, the signal above background in each hit in the collection is tabulated. The slope m is obtained from a straight line fit to the log of the distribution as depicted in Figure 7. This measurement fixes the average DN per photon detected, since the statistical mean of the single-photon response $P_1(n)$ is just

$$\langle n \rangle = \frac{\int n P_1(n) dn}{\int P_1(n) dn} = 1/m. \tag{9}$$

The raw data for the pulse-height analysis were drawn from the XRCF test imagery used in the PSF study. In the many hundreds of images collected, there were thousands of isolated hits that had been wide-angle scattered far from the point-source center. Pulse-height analysis of individual photon hits could be reliably performed above 800 V. The results are plotted as symbols in Figure 6 (right). The solid line shows the power law response (corrected for MCP quantum efficiency) according to the laboratory integrated photon analysis, which has the same slope as the single-photon estimates but is consistently 30% above them. This shift is interpreted as due to the DN contained in the halo, which is below the noise level in the individual photon hits but which rises to detectable levels when the entire CCD is flooded with photons to several hundred DN/pixel signal strength during integrated photon testing. This substantial halo DN content is consistent with the PSF analysis, which suggests ∼1/3 of the total signal resides in the halo (see Figure 1). Allowing for this halo correction, the single-photon analysis thus confirms the internal consistency of the integrated-photon calibration detailed above.

Putting this all together, the best mean fit to the SXI detector response is given by

$$\mathrm{DN/photon}_{\mathrm{detected}} = 9.0 \times 10^{-6} \times \exp\left(0.0181 \times V_{\mathrm{MCP}}\right). \tag{10}$$

By invoking one additional statistical relation in conjunction with the above analysis, we can obtain an estimate of how many photons it takes to produce a given DN level in an SXI image. It can readily be shown (see Appendix) that multiple hits in a given area of the CCD produce a collective statistical response given by the Poisson probability function,

$$P_j(n) = \frac{(mn)^{j-1}}{(j-1)!} P_1(n), \tag{11}$$

where $P_1(n)$ is the probability of getting n detector counts with a single photon hit and $P_j(n)$ is the probability of getting n detector counts with j photon hits. The peak of the Poisson distribution, which corresponds to the most probable number of photons producing the measured n occurs at

$$j_{\max} = mn + 1. \tag{12}$$

This relation also expresses the inherent linearity of the detector.

Using (9), (10), and (12), we can determine as a function of V_{MCP} the most likely number of detected photons needed to produce a given DN level in uniform, extended solar features. For example, Figure 8 indicates that ~5200 photons

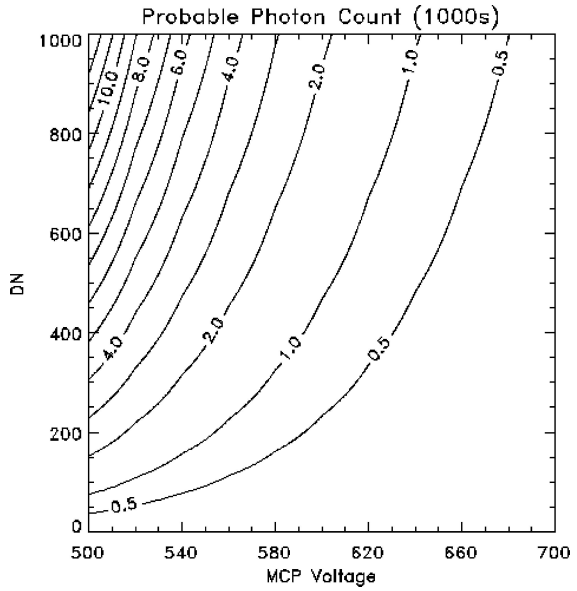

Figure 8. The most probable number of detected photons contributing to a given DN level, as a function of MCP voltage.

TABLE V
SXI filters.

Designation	Nominal composition
prefilter	3000 A Poly, 1250 Å Al, 1000 Å Ti
OPEN	–
P_THN_A(B)	3000 A Poly, 1000 Å Al, 800 Å Ti
P_MED_A(B)	5000 A Poly, 1500 Å Al, 800 Å Ti
P_THK	8000 A Poly, 3000 Å Al, 800 Å Ti
B_THN_A(B)	Be 12.7 (17.0) μ
B_MED	Be 25.4 μ
B_THK	Be 50 μ
UV	Fused silica diffuser
RDSH	Stainless steel, 7.9 mm

must be detected to produce full-well exposure in OPEN filter patrol images, which are run typically at 550 V on the MCP. Except at the lowest count rates ($\text{photon}_{\text{detected}} \leq 100$) the nominal uncertainty is given by $\sqrt{2 \times \text{phot}_{\text{detected}}}$ (see Appendix for derivation). Thus the full-well 550 V exposures represent about 5200 ± 102 photons detected.

A discussion of statistical considerations to be weighed in applying the above measures of detector photon response to SXI images is given in the Appendix.

5.3. Pre-filter and filter responses

The SXI filter complement includes an entrance or "pre-filter" (which is mounted in six annular segments in front of the mirror assembly) and 12 analysis filters (housed in circular slots in a filter wheel near the focal plane).

In Table V OPEN denotes the filter wheel position containing no analysis filter, hence allowing the widest possible bandpass. "Poly" refers to the polyimide substrate, for which the composition is $C_{17}\,H_5\,O_4\,N_3$. The designations "A" and "B" distinguish duplicates of the thin and medium polyimide and thin beryllium filters. The transmissions of the filters were measured during fabrication, and these data were re-verified at discrete wavelengths during XRCF testing. Figure 9 (left) shows the transmission of the pre-filter, and the right panel depicts the optical system effective area using each of the analysis filters.

5.4. Response to solar emissions

5.4.1. *Performance Comparison with other Instruments*

A comparison of the SXI spatial and spectral properties to previous grazing-incidence instruments is presented in Figure 10. At left, it is seen that the overall

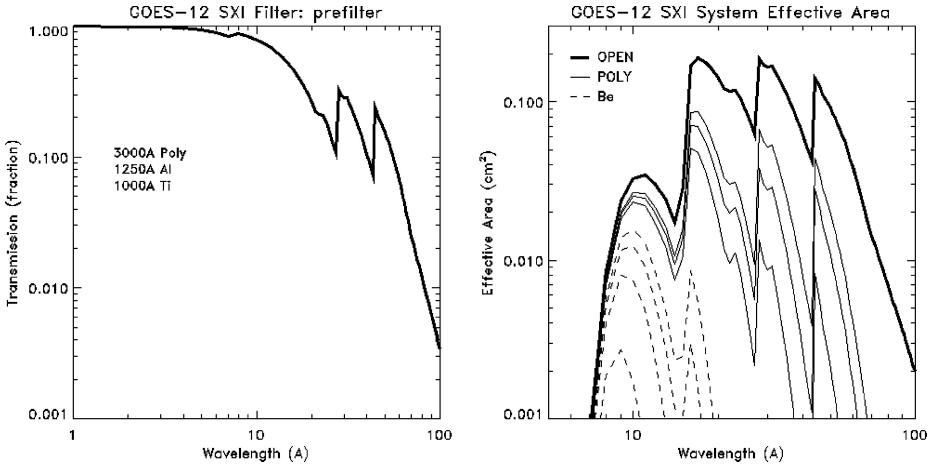

Figure 9. Transmission (*left*) of the pre-filter and effective areas (*right*) of SXI analysis filters. The latter include convolution of the pre-filter, mirror, and detector spectral responses. The extra beryllium curve (dashed) is for the backup ("B") thin Be filter, which is significantly thicker than the primary ("A").

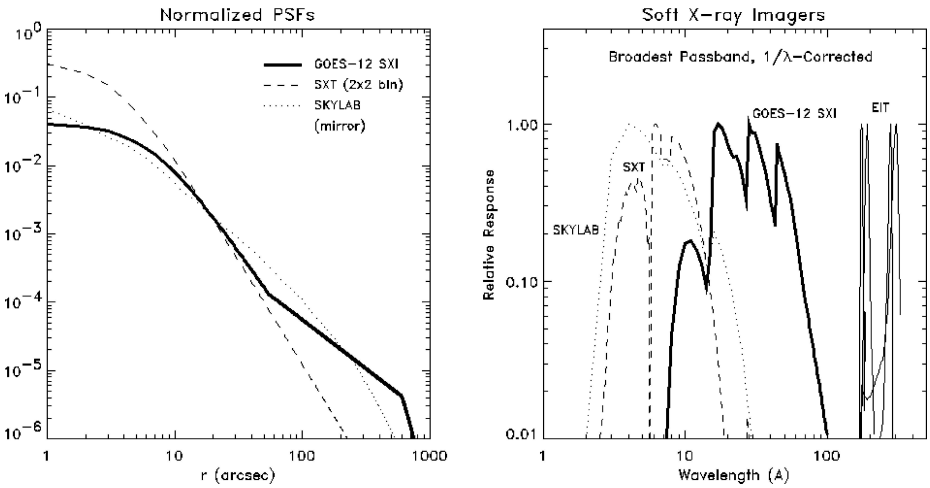

Figure 10. Comparison of SXI PSF (*left*) and spectral response (*right*) to earlier grazing-incidence X-ray telescopes. The discrete passbands for the normal-incidence SOHO/EIT instrument are also shown at right. The PSF of the SXT refers to the 2×2 binned full-disk images; that for EIT is similar. All responses have been normalized to the peak spectral response of each instrument; the plot thus does not show overall differences in throughput.

PSF of SXI is more similar to that of *Skylab* S-054 (Vaiana *et al.*, 1977) than that of *Yohkoh* SXT, whereas the spectral passband (right) extends to much longer wavelengths than in the other two instruments. A key element of the spectral response plot is that the wavelength response of the detector (an additional $1/\lambda$ factor in the

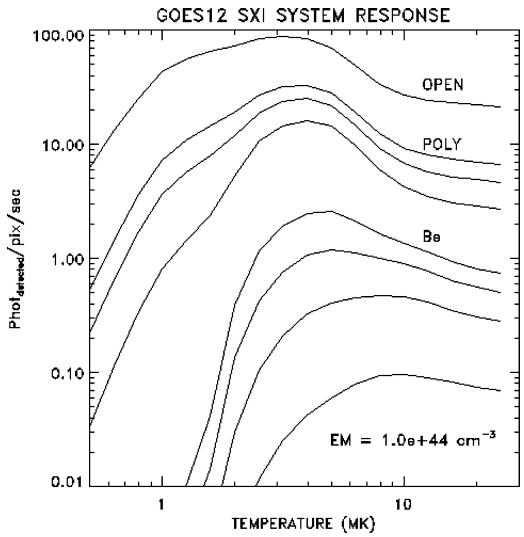

Figure 11. SXI system response as a function of coronal temperature, for fixed emission measure.

case of the direct CCD detector for SXT, film-based response for *Skylab*) has been taken into account.

5.4.2. *System Throughput for X-ray Corona*

The SXI system throughput has been computed by convolving the full instrument response with a representative solar emission model. Figure 11 shows the SXI response to solar plasma emissions over a range of coronal temperatures, as calculated from a standard spectral emission model (Mewe, Gronenschild, and Oord, 1985). The OPEN filter position offers excellent response between 1 and 4 MK, while the denser filters shift and narrow the response about progressively higher temperatures.

The SXI response can also be computed for typical solar features. Table VI lists a compilation of temperatures and emission measures for a variety of coronal features, as gleaned from the literature.

Table VII presents the photons detected per second at the focal plane for the features characterized in Table VI.

This information, coupled with the detector response material in Section 5.2, provides the current best estimate for SXI absolute response. A rocket underflight using a calibrated spectrometer is scheduled for 2004 to refine the response estimate further.

5.4.3. *Filter Ratios and Coronal Temperatures*

For uniform isothermal coronal plasma, an estimate of the temperature may be inferred from the ratios in the observed emission (e.g., Sturrock, Wheatland, and Acton, 1996). SXI optical characteristics coupled with the Mewe emission model

TABLE VI
Emission characteristics of select solar features.

	Feature	Temp (MK)	Emission measures (10^{44} cm^{-3})	Flux 6 – 60 Å (phot cm^{-2} s^{-1} arcsec^{-2})
1	Coronal hole min	1.3	2.00E−02	0.75
2	Coronal hole avg	1.8	6.60E−02	2.94
3	Coronal hole max	2.1	2.10E−01	10.5
4	Large coronal loop	2.1	6.00E−02	3.00
5	X-ray bright point	1.8	7.00E−01	31.3
6	Active region	2.5	3.00E+01	1.67e+03
7	Active region core min	2.5	3.60E+00	2.03e+02
8	Active region core avg	3	3.70E+00	2.18e+02
9	Active region core max	3.5	3.80E+00	2.24e+02
10	Post flare loop	7.0	3.00e+02	9.11e+03
11	Long-duration event	7.5	1.00e+04	2.77e+04
12	C flare	6	1.10E−01	9.90e+02
13	M flare	17	2.00E+04	3.50e+05
14	X flare	20	1.00E+05	1.69e+06

TABLE VII
SXI photon flux detection rate ($\text{phot}_{\text{detected}}$ s^{-1}) for select solar features.

	Open	P_thin	P_med	P_thick	Be_thin	Be_med	Be_thick
1	1.14E+00	2.28E−01	1.20E−01	3.13E−02	3.04E−04	3.56E−05	4.60E−06
2	4.46E+00	1.06E+00	6.20E−01	2.25E−01	1.15E−02	1.61E−03	2.40E−04
3	1.59E+01	4.47E+00	2.91E+00	1.42E+00	1.44E−01	1.95E−02	2.81E−03
4	4.58E+00	1.29E+00	8.38E−01	4.09E−01	4.14E−02	5.63E−03	8.08E−04
5	4.74E+01	1.13E+01	6.59E+00	2.39E+00	1.23E−01	1.71E−02	2.55E−03
6	2.53E+03	8.26E+02	5.81E+02	3.32E+02	4.41E+01	6.92E+00	1.05E+00
7	3.07E+02	1.00E+02	7.05E+01	4.02E+01	5.35E+00	8.39E−01	1.27E−01
8	3.30E+02	1.20E+02	8.87E+01	5.51E+01	8.91E+00	1.65E+00	2.67E−01
9	3.39E+02	1.31E+02	9.98E+01	6.48E+01	1.17E+01	2.33E+00	3.85E−01
10	1.38E+04	5.88E+03	4.68E+03	3.34E+03	1.15E+03	3.85E+02	8.37E+01
11	4.20E+05	1.78E+05	1.42E+05	1.02E+05	3.78E+04	1.33E+04	2.95E+03
12	1.50E+06	6.15E+05	4.85E+05	3.52E+05	1.61E+05	6.47E+04	1.50E+04
13	5.31E+05	2.04E+05	1.57E+05	1.10E+05	4.91E+04	2.08E+04	5.22E+03
14	2.55E+06	9.63E+05	7.35E+05	5.09E+05	2.23E+05	9.54E+04	2.46E+04

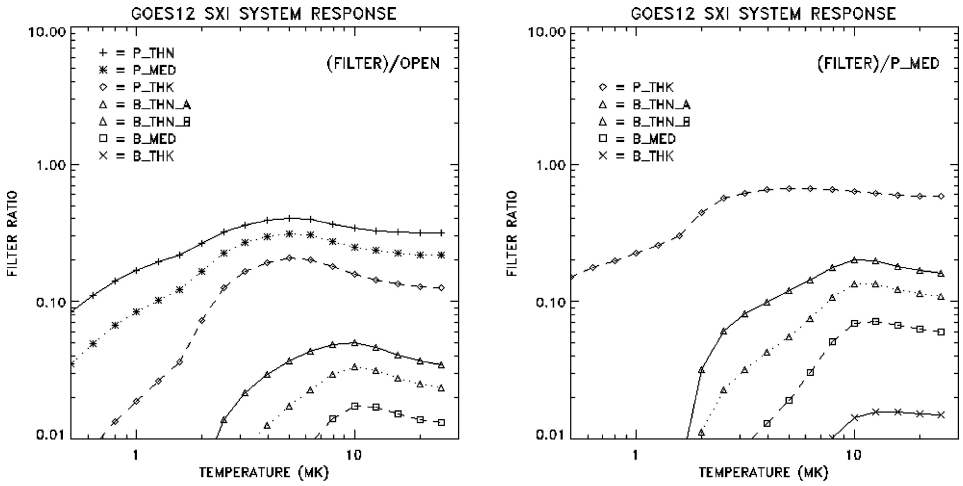

Figure 12. Representative predicted SXI filter ratios used for temperature diagnostics.

have been used to assess the utility of SXI filter ratios for determining coronal temperatures. Figure 12 shows the resultant curves for two key patrol filter selections. SXI offers good temperature diagnostics over a range of coronal temperatures, although the utility of the filter combinations at the higher temperatures is limited due to low signal strengths obtainable within the maximum 3-s imaging interval. Moreover, the extent to which the potential of the ratios is compromised because of the scattered light contamination from the halo effect remains to be determined.

6. Image Corrections

A number of corrections must be applied to the raw images to account for various instrumental factors that would otherwise affect image quality and/or utility. All the corrections described below are applied routinely to SXI Level-1 images, except that of the three flat-field components discussed below, only the vignetting correction is currently employed.

6.1. BACKGROUNDS

Several times per day during normal operations, dark images are taken with the radiation shield in place, with 0 volts on the MCP, and for a few specific integration times in the operational range (1 ms – 3 s). CCD line advance is ON during these exposures. These images include the dark current contribution from thermal noise and a bias current providing a 4 –5 DN offset above the nominal zero DN level.

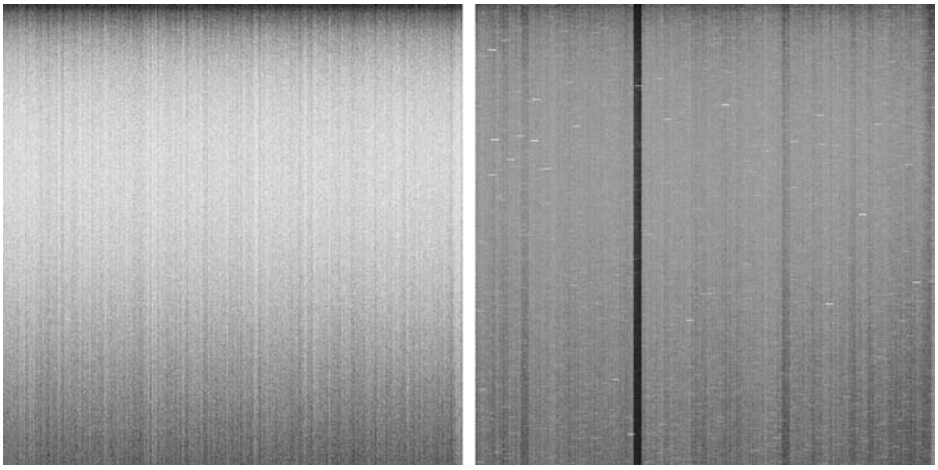

Figure 13. Reference background images: 1 ms exposure (*left*); 3 s exposure (*right*). The short white dashes and thick dark stripes in the longer exposure arise from hot pixels and the effects of bad reference pixels being smeared horizontally by the CCD line advance.

Dark images can be taken using the hardware log scaling option and at operational MCP voltage settings, but these are for special purposes only.

Experience gained during PLT demonstrated that image-to-image variations due to line noise fluctuations, cosmic ray hits, and random defects militate against using the most recent dark images for operational background subtraction. SXI dark correction is therefore based upon the use of "reference background (BG)" images constructed from a suitable average of dark images taken over a period of time. These reference BGs account for bias and dark current variations as a function of exposure time and CCD temperature, which can vary over the range $-31\,^{\circ}$C to $-4\,^{\circ}$C. The reference BGs are calculated and stored in floating point format to avoid digitization errors. For SXI applications, the reference BGs are generated at $1\,^{\circ}$C thermal increments and the collection is updated periodically to track potential secular variations in the instrument. Note that this correction method does not compensate completely for line noise in any particular solar image.

Figure 13 shows typical 1 ms (left) and 3 s (right) reference background images at a CCD temperature of $-21\,^{\circ}$C. Both darks are almost flat (typically, ± 1 DN fluctuations) about a mean DN of about 5. The long-wavelength top-to-bottom gradient in intensity (most evident in the 1 ms reference BG) is probably due to broad thermal variations across the CCD face. The vertical striping (also seen in Figure 2) is an artifact of the CCD readout, in which the charge in any pixel in a CCD column is referenced to that in a special shielded pixel at the base of that column. Since the charge in the shielded pixel has a random noise level, the values in each CCD line bob up and down relative to neighboring lines within a given image as well as from image to image. At 1ms integration time this effect is minimal, but for dark exposures of longer duration additional effects appear. Not only does the

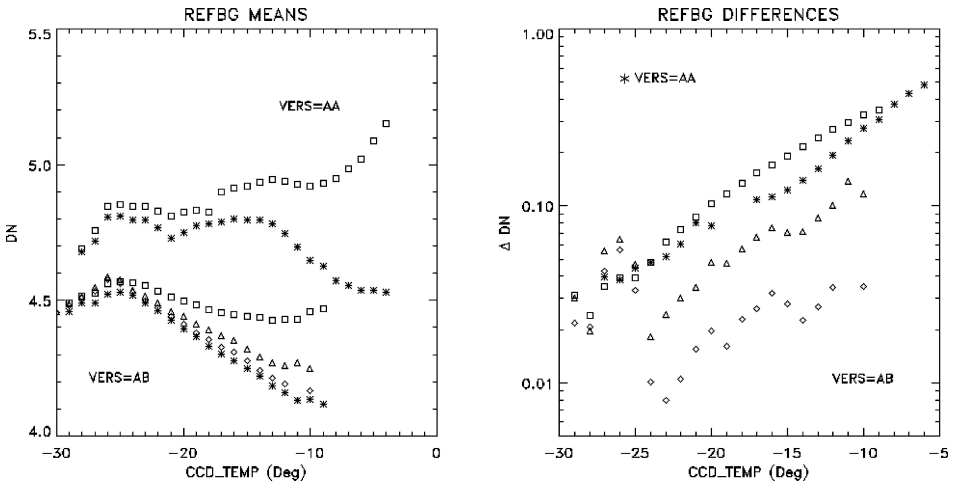

Figure 14. Thermal and secular variation in reference background images. The sets of curves labeled "AA" are data from PLT in late 2001, those labeled "AB" are from the reactivation period in early 2003. The *left panel* shows the mean DN in the reference backgrounds in 1 °C bins, for a variety of exposure times. *Open symbols* in the *right panel* show the difference between (3.0, 1.1, 0.334) s darks and the 1 ms reference dark image for the AB set at that CCD temperature. The 3 s minus 1 ms difference for the AA set is also shown (∗).

overall noise level increase (see Figure 14 below), but also small current leaks in some of the reference pixels cause noticeable drops in the output DN in a few of the columns. This effect, coupled with the CCD line advance (3 s BGs undergo nine line shifts during the exposure), leads to the stepped horizontal smearing seen in the image at right.

The thermal noise level in the detector varies linearly with exposure time and exponentially with temperature. In Figure 14 (left), the top two curves show the mean DN from 3 s and 1 ms reference BGs collected during PLT ("VERS AA") and the lower four curves (1 ms, 334 ms, 1.11 s, and 3 s) are from the SXI reactivation period ("VERS AB"). There is clear indication of secular variations in dark properties. The figure at right shows explicitly the exponential dependence upon temperature. These plots also show that the variation in the bias level is complicated, with a break in behavior near −25 °C.

6.2. FLAT FIELD

The flat-field correction for SXI may be computed as the product of three pixel-by-pixel expressions that account for image defects and distortions according to wavelength. That is, the corrected signal strength is related to the raw, dark-current subtracted signal as

$$\mathrm{DN_{corr}} = \mathrm{DN_{raw}}/(\mathrm{C1} \times \mathrm{C2} \times \mathrm{C3}), \tag{13}$$

where C1 accounts for long spatial scale ($\geq$100 pixel) error, C2 for mid-frequency (30–100 pixel) error, and C3 for short spatial scale ($<$30 pixel) error. (For exposures $>$0.333 s, horizontal smearing of each of these flat fields due to the CCD line advance must be accounted for.) Currently, only the long wavelength correction C1 is applied operationally.

Vignetting is the primary source of long-wavelength error in SXI. A direct measure of the vignetting is drawn from the relative variation in total measured intensity in pre-launch point images taken over a range of field angles about the optical axis. Although vignetting in Wolter I optics has been characterized as a radially symmetric linear decline with distance from the optical axis (e.g., VanSpeybroeck and Chase, 1972), a good fit to the collected data may be expressed as

$$\mathrm{C1} = 1.0 - 2.55 \times 10^{-6} \times ((x - 258)^2 + (y - 258)^2), \tag{14}$$

where x and y are the horizontal and vertical pixel numbers, with pixel (0, 0) marking the lower left corner of the image. The SXI vignetting amounts to $\sim$7% correction at 15 arcmin distance from the optical axis.

The mid-frequency correction C2 is dominated by a phenomenon known as the "ghost" image. This artifact is evident under illumination by the UV lamp and by solar X-rays (Figure 15). Both means of measuring the effect have difficulties. The intensity and illumination pattern of the UV lamp varies considerably, and the detector responds differently to UV photons than to X-ray photons. In addition, X-ray calibrations require special pointing operations and low solar activity. Nevertheless, combined X-ray and UV imagery does establish that the ghost image represents a true localized relative enhancement (as opposed to loss) in sensitivity, and that the peak magnitude of the effect is in the range 10–20%. The physical mechanism for the effect is under study, with the leading candidate being a selective scrubbing

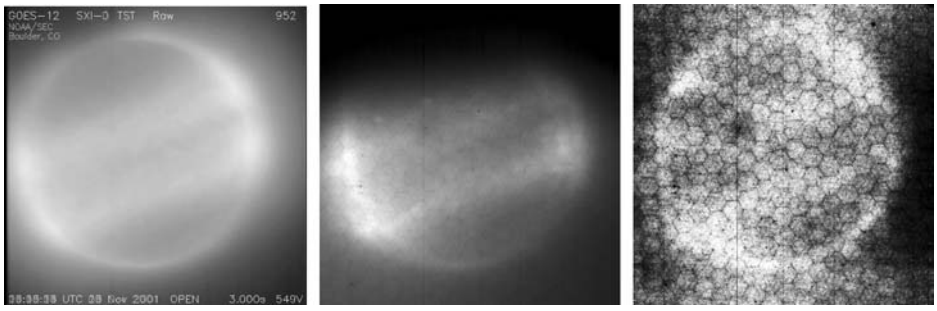

Figure 15. The "ghost" image effect. From left, the average of all 3-s patrol images taken with the OPEN filter position in 2001, a UV lamp-illuminated image taken during PLT, and a partially processed composite of X-ray images obtained in fast-scan mode during SXI reactivation testing in February 2003.

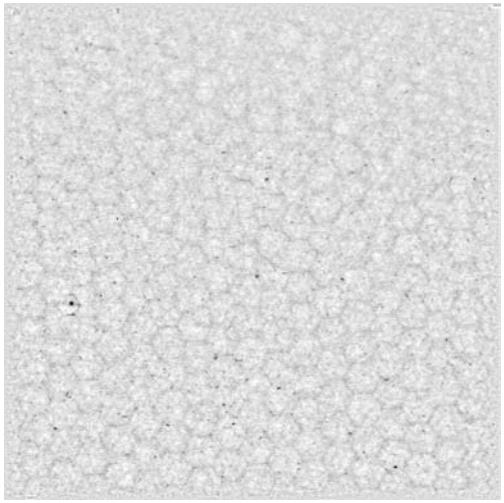

Figure 16. Map of small spatial scale defects (C3 correction) derived from UV lamp test imagery. The MCP hex pattern is apparent, as are defective pores (tiny black dots) and other artifacts.

of residual contaminants in the MCP channels by the electron cascades stimulated during normal operations.

The small spatial scale error includes contributions from hot pixels, the MCP hex and pore pattern, dust motes, and various CCD manufacturing defects. A working C3 correction can be obtained from UV lamp imagery. Dark-subtracted composites of a collection of UV images are smoothed with a 29-pixel median filter, which is then subtracted from the composite to extract the short-wave component. As shown in Figure 16, the hex and pore pattern of the MCP is readily visible, as are other artifacts, such as the fine ring feature just above and to the right of CCD center. Hot pixels are also present, but are hard to discern in this reproduction. With the exception of several defective pores, the amplitude of most of the features in Figure 16 is of the order of a few percent. A C3 correction may be defined on the basis of this pseudo-image. An important element of the correction process is to clip the correction where the intensity of the target solar image approaches the noise level, lest a reverse image of the hex pattern and other low-amplitude defects be spuriously imposed. Operational application of the C3 correction awaits reduction of the latest UV lamp calibration images.

During the SXI reactivation period a special set of X-ray images was obtained to address flat-fielding issues at all spatial scales. For these tests, the GOES spacecraft solar array was mechanically slewed in the east-west direction to scan SXI rapidly across the Sun. During the scan, the CCD was exposed for 40 s, with the thin polyimide filter in place to block the off-band light leak (see next section). Scans were executed at five NS pointing angles to assure even coverage of the CCD, and special dark images were obtained to support the analysis. Preliminary

reduction of the data confirms the presence of the ghost image under X-ray illumination (Figure 15, right), as well as the MCP hex pattern and other artifacts. Further processing of these data will lead to a functional mid-wavelength correction (C2), and to improvements in the flat-fielding at other spatial scales. Also, a set of solar images suitable for Kuhn-Lin flat-field analysis (Kuhn, Lin, and Loranz, 1991) has been taken and will contribute to the ongoing calibration of SXI imagery.

6.3. OFF-BAND LIGHT LEAK AND CORRECTION

When high-voltage imagery was resumed upon SXI reactivation on 22 January 2003, a bright (∼150 DN peak) diffuse feature was found in the lower left corner of the 3-s OPEN exposures and a bright band (∼25 DN peak) was discovered across the lower part of the 15-msec OPEN images. These phenomena had no counterpart during PLT. Their origin has since been traced to a leak consisting of visible and near UV off-band light, to which the phosphor in the detector stack is sensitive. There are two possibilities for the root cause: either the spontaneous development of a pinhole in the prefilter (see Section 5.3), or a breach in the optical system forward of the filter wheel, perhaps related to a micrometeorite hit recorded on GOES 12 about 2000 UT on 19 January 2003. That impact was large enough to be detected via HASS and Earth sensors as a rolling up and down motion of the entire spacecraft. The polyimide and beryllium analysis filters (Table V) block this off-band light, so that images taken with them in place are not affected by the leak.

The magnitude and pattern of the leak appears to be a function of pointing and instrument temperature, and the precise relation continues to be investigated. The OPEN filter image effects come from a combination of light-leak signal imprinted onto the CCD during pre-image flush and from direct long-wavelength exposure sustained during image integration. Quantitative knowledge of the light-leak properties has been built up via dedicated test sequences as well as by the ongoing collection of special 0-volt OPEN images, which isolate the light-leak contribution. (With no voltage on the MCP, there is no cascade effect and the entire signal comes from the light leak response.) The properties of the light leak appear to be stable from the time of SXI reactivation in January 2003 until the entrance filter failure in November 2003.

Analysis of the light leak imagery suggested that a simple correction strategy would suffice to eliminate 95% of the spurious light for typical pointing conditions. From a large archive of special 0-volt OPEN light-leak background images collected by SXI, the one having most nearly the same pointing and CCD temperature as the current solar image is selected. The selected image is subtracted from the solar image to provide *both* dark and light-leak corrections. The strategy is illustrated in Figure 17. Its performance is monitored as part of routine calibrations.

Figure 17. Illustration of visible light correction scheme.

6.4. ENERGETIC PARTICLE RESPONSE

The geosynchronous GOES-12 orbit affords SXI little protection against cosmic rays and solar proton events, relative to that experienced by L1 platforms. Moreover, geosynchronous instruments are additionally subjected to very energetic (>1 Mev) electrons from the terrestrial radiation belts (R. Zwickl and T. Onsager, *private communication*). Particle tracks are often seen in SXI imagery during proton storms, as shown in Figure 18. Unique to the SXI response, however, is the dark vertical striping often evident during such events. The stripes stem from hits to the CCD reference pixels, which cause the electronics to subtract excessive signal from all the pixels in affected CCD lines. The SXI mirror is also capable of focusing low-energy protons populating the magnetosphere. Such proton focusing has led to degradation of the Chandra X-ray instrument response (O'Dell *et al.*, 2000), but

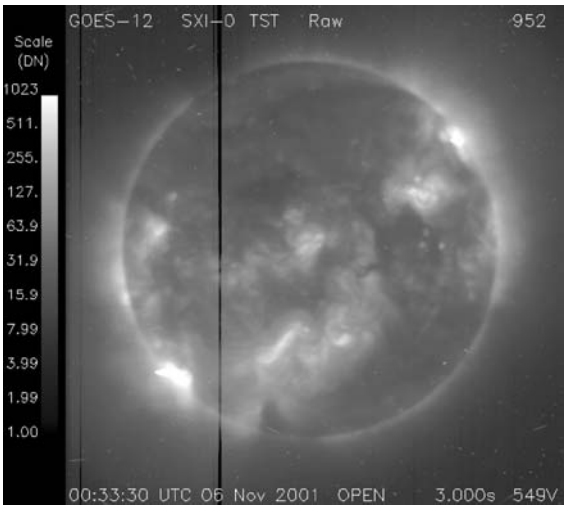

Figure 18. SXI image taken during a proton storm, showing energetic particle tracks and dark vertical striping due to hits sustained by CCD reference pixels.

the effect is much reduced in SXI since the mirror graze angle is much steeper and the MCP absorbs most of the incident protons without initiating a cascade.

6.5. Absolute pointing knowledge and plate scale

Errors in SXI pointing are due to limitations on the accuracy of the pointing platform control and coupling of the spacecraft and orbital dynamics. The Sun is typically centered within the field of view to ± 3 arcmin. Uncertainties in pointing knowledge are much smaller and are caused by changing angular offsets between the HASS and SXI due to optical bench thermal strains, orbital inclination errors, and statistical errors in HASS measurements. This subsection addresses each of these error sources in turn.

Optical bench thermal strains dominate the pointing knowledge uncertainty for SXI. During non-eclipse operations, temperatures change gradually and the offset between the HASS and SXI optical axes varies about a mean value by about ± 8 arcsec over seasonal time scales. This variation is highly correlated to the HASS sensor temperature and indicates changes in pointing of about 1 arcsec per degree Kelvin. Smaller variations happen on daily (orbital) timescales. During eclipse season, the spacecraft is plunged suddenly into darkness for up to 70 min and then suddenly again into direct sunlight. The sudden, sharp thermal gradients cause alignment offsets that cannot be directly extrapolated from observations of slow, seasonal thermal changes. The post-eclipse pointing errors are predominantly along the north-south direction with the HASS data typically indicating a Sun-center position north by twenty or more arcsec of the true Sun-center position for several hours. Work is underway to incorporate a correction to SXI pointing meta-data based on thermal parameters.

As explained in Paper 1, the solar image is rotated about the optical axis due to coupling between the SXI pointing platform, spacecraft attitude, and spacecraft orbit. Orbit management limits inclination to $\pm 0.5^\circ$, which results in a maximum uncertainty of $\pm 0.5^\circ$ in image roll about the Earth–Sun line. This is equivalent to 1.8 pixels (9 arcsec) at the solar limb. Knowledge of the orbital ephemeris allows for a correction to the value, but has not yet been implemented operationally.

Finally, since pointing knowledge for each SXI image is taken as the mean of many HASS measurement during the exposure, examination of the standard deviation of those measurements describes the statistical uncertainty in pointing knowledge. Typically, the standard deviation is ± 2 arcsec. This is consistent with digitization noise since the minimum HASS angular measurement increment is 3.9 arcsec.

If systematic errors in the SXI pointing knowledge can be corrected, the achievable accuracy should only be limited by the HASS statistics of ± 2 arcsec. However, at this time these corrections are still under study. Thus, pointing knowledge

uncertainty in standard operational products is of the order ±10 arcsec (±20 arcsec immediately following eclipses). While adequate for basic, automated, operational flare location, this accuracy is insufficient for use when performing detailed co-registration with other image data sets. It is therefore recommended that for such studies, that a quasi-static (time scale of hours) offset in pointing knowledge be determined from comparing manual limb fit results with SXI pointing information. This technique should be able to achieve accuracies of better than ±5 arcsec.

A result of studies on SXI pointing knowledge is confirmation of the SXI plate scale. The measured plate scale is 5.030 ± 0.015 arcsec per pixel whereas the predicted plate scale is 5.014 arcsec. The uncertainty on the measured plate scale reflects only statistical errors. Systematic errors due to miss-estimation of the solar limb location are not included. Thus, we take the design value of 5.014 arcsec per pixel as the actual flight value.

6.6. IMAGE TIMING KNOWLEDGE ACCURACY

The SXI operates as a real-time system, broadcasting its data 'live.' All delays due to digital buffers and propagation have well known and unchanging uncertainties. While the onboard clock is accurate enough to be used for control of image scheduling, its drift rate would make uncertainties in time tagging relatively large compared to ground based, telemetry receipt time tagging.

The digital system delays and the associated uncertainties have been examined in detail. For instance the delay from the completion of integration to the incorporation of the last HASS measurement ranges from 0 to 16 ms, but has an uncertainty of only 0.064 ms. Delays considered in ground systems include bit synchronization delays among others. The only unknown delay is the interrupt latency of the ingest computer, but it is likely to be very small. All of the above make up only minor sources of uncertainty.

The two major sources of uncertainty are the RF propagation delay from the spacecraft to the ground station antenna and the uncertainty in the ground system timeserver accuracy. The RF propagation delay uncertainty is due to the fact that time tagging computations use the nominal spacecraft location and not its actual location derived from ephemeris data. The GOES 12 is generally allowed to drift up to ±0.5° in latitude and longitude from its nominal location of 75° west longitude and 0° latitude. This translates into timing uncertainties of up to 0.15 ms in the worst-case scenario.

The timeserver system itself receives timing data from WWVB, GOES, and GPS with an accuracy of 1 ms. The ingest-preprocessing host is periodically updated with the timeserver time. The local time kept on the ingest-preprocessing host is 'smoothed' to prevent the undesirable effect of time jumping backward due to an update from the timeserver. This smoothed time is used for the time-tagging of SXI images. In addition to the smoothed time, the 'delta' time to the non-smoothed

time is provided as well as the time of the last update to the ingest-preprocessor time.

It is clear the single most important source of image timing uncertainty is attributable to errors/drift in ground system clocks and network errors resulting in missed timeserver updates. Given these error sources and the timing data kept for SXI images, it is possible to statistically evaluate the likely uncertainties in timing for SXI data. For the PLT period, it was found that 99.99% of the time the error was less than 40 ms. For a sample period in late 2003, after the timeserver 'minimum tick' had been reduced from 10 ms to 2 ms, 99.99% of the time the error was less than 17 ms.

7. Summary

The presentation above provides SXI data users with a solid understanding of the observational characteristics of the instrument and provides researchers with the kind of quantitative calibrations needed to conduct advanced analyses of the imagery. To these ends, we have detailed the performances of the instrument components and the combined system, as are best known to this date. In addition, we have described at some length image correction procedures currently applied to production images in the hope of guiding further improvements.

The performance capabilities of the base GOES-12 SXI instrument suffice to carry out its fundamental mission of monitoring evolving coronal X-ray structures related to space weather forecasting. Its moderate spatial resolution is more than adequate for tracking large-scale solar features associated with geospace disturbances, and its spectral passband – nicely spanning the gap between previous soft X-ray imagers and the current EUV observations of SOHO/EIT – enables observation of structures across a broad range of coronal temperatures. The strong suit of the GOES-12 SXI instrument is its unprecedented cadence and continuity of observation, which allows the evolution of relevant solar features to be followed with the consistency and regularity needed to promote new understanding of many solar physical processes.

8. Epilogue

The hardware degradations suffered by SXI in 2003 are detailed in Paper 1. These include an anomaly in the high-voltage MCP supply system and the loss of one of the six annular entrance filter segments. The first problem resulted in the imposition of a 500 V limit on MCP operations, and the second precluded the use of the OPEN filter position. In addition, a small amount (a few DN) of offband light now appears at the focal plane in long ($\geq$3 s) exposures in some filter positions. The system response characterized here otherwise still applies, albeit that the instrument now operates over only a small fraction of the intended parameter space.

The performance properties described in this paper, including additional plots and digital data files, are accessible on the SXI website at *http://www.sec.noaa.gov/sxi/ScienceUserGuide.html.* Updates will be made as new calibration information becomes available.

Appendix: Photon Statistics for SXI Images

There are three basic contributors to the uncertainty in the photon count in a raw SXI image: photon noise associated with the solar source, Poisson noise associated with the MCP detector stack, and background noise, which includes dark current, quantization noise, and line noise (which stems from the reference pixel structure of the SXI CCD.)

The uncertainty in the source photon noise scales with the square root of the number of photons collected. The uncertainty in the number of electrons generated by the SXI detector is more complicated to assess. A simple model for the response of the detector to a uniform, extended solar source can be obtained as follows.

As stated in the text (8), the probability that a single photon will produce n counts at the CCD is given by

$$P_1(n) = m\, e^{-mn}, \tag{A1}$$

where m is a function of V_{MCP}.

To determine the statistical response of multiple, overlapping hits on some given area of the detector, consider first the probabilities involved in two photon hits. To record n counts for the two hits, if the first hit produces k counts the second must produce $n - k$ counts. The joint probability P_2 is then the sum (here represented for expediency as a continuous integral) of all the combinations of k and $n - k$ summing to n:

$$P_2(n) = \int_0^n \mathrm{d}k\, P_1(k) P_1(n-k), \tag{A2}$$

which integrates to

$$P_2(n) = m^2 n e^{-mn} = mn\, P_1(n). \tag{A3}$$

Likewise for three hits, if the first produces k counts, and the second produces $l \leq (n - k)$, the third must yield $n - k - l$. The net probability is therefore

$$P_3(n) = \int_0^n \mathrm{d}k \int_0^{n-k} \mathrm{d}l\, P_1(k) P_1(l) P_1(n-k-l), \tag{A4}$$

which works out to

$$P_3(n) = \frac{1}{2}(mn)P_2(n). \tag{A5}$$

Similar consideration of four hits, etc., establishes the series as the Poisson distribution via the well-known recurrence relation

$$P_j(n) = \frac{mn}{j-1}P_{j-1}(n). \tag{A6}$$

Given that Poisson statistics govern the detector response, the uncertainty in the number of photons collected therefore varies as the square root of the most probable number of contributing photons. This uncertainty is essentially the same as that for the source.

The above development, together with estimates for the background noise, enables us to construct a noise model for SXI imagery. The model is developed in terms of the DN collected in the detector, since the background noise is easier to approximate that way. Let (10) define the detector gain factor, g, which represents the conversion from the number of detected photons to the output DN, i.e.,

$$g = 9.0 \times 10^{-6}\, \mathrm{e}^{0.0181}\, V_{\mathrm{MCP}}. \tag{A7}$$

We can then write the signal-to-noise ratio (SNR) as

$$\frac{\mathcal{S}}{\mathcal{N}} = \frac{g N_{\mathrm{det}}}{\sqrt{\mathcal{N}_{\mathrm{src}}^2 + \mathcal{N}_{\mathrm{det}}^2 + \mathcal{N}_{\mathrm{bg}}^2}}, \tag{A8}$$

where $\mathcal{S}$ is the signal in DN, $\mathcal{N}$ is the noise in DN, and N_{det} is the number of detected photons. The three terms in the square root account respectively for the source and detector photon noise (for each of which the noise is $g\sqrt{N_{\mathrm{det}}}$) and the background noise. The latter can be expanded as

$$\mathcal{N}_{\mathrm{bg}}^2 = \mathcal{N}_Q^2 + \mathcal{N}_D^2 + \mathcal{N}_L^2 = 2\big(\mathcal{N}_Q^2 + \mathcal{N}_D^2\big), \tag{A9}$$

where $\mathcal{N}_Q$ is the quantization noise (including read noise), $\mathcal{N}_D$ is the dark or thermal noise (which is really exposure-time dependent), and $\mathcal{N}_L$ is the line noise, which is actually a composite of $\mathcal{N}_Q$ and $\mathcal{N}_D$ that is reapplied through the reference pixels. Following Schagen (1974), we express the sum of the photon source and detector noise terms as

$$\mathcal{N}_{\mathrm{src}}^2 + \mathcal{N}_{\mathrm{det}}^2 = (g N_{\mathrm{det}})^2 F_{\mathrm{MCP}}, \tag{A10}$$

where F_{MCP} is a multiplicative factor accounting for noise in the MCP. (Writing the photon noise contributions this way facilitates the analysis, as we shall shortly see.)

The SNR equation may finally be written as

$$\frac{\mathcal{S}}{\mathcal{N}} = \frac{g N_{\rm det}}{\sqrt{N_{\rm det} g^2 F_{\rm MCP} + 2\left(\mathcal{N}_Q^2 + \mathcal{N}_D^2\right)}}. \tag{A11}$$

With suitable specification of $F_{\rm MCP}$ and the background noise terms, this equation can be solved directly for the $N_{\rm det}$ needed for a given SNR, e.g., SNR = 3.0. Multiplying out the denominator on the right, squaring and collecting terms, we finally get the quadratic

$$g^2 N_{\rm det}^2 - \left(\frac{\mathcal{S}}{\mathcal{N}}\right)^2 g^2 F_{\rm MCP} N_{\rm det} - 2\left(\frac{\mathcal{S}}{\mathcal{N}}\right)^2 \left(N_Q^2 + N_D^2\right) = 0, \tag{A12}$$

which can be solved for $N_{\rm det}$ by standard means.

In the simple case where we ignore the background noise and the detector noise is assumed to scale like the source noise, $F_{\rm MCP} = 2.0$ and the above relation reduces to

$$\left(\frac{\mathcal{S}}{\mathcal{N}}\right) = \sqrt{\frac{N_{\rm det}}{2}}. \tag{A13}$$

The uncertainty in the net photon count is then $\sqrt{2N_{\rm det}}$.

In practice, $F_{\rm MCP}$ may vary from 2.0 (optimistic case) to 5.0 (pessimistic) depending upon the details of the MCP fabrication and operating voltage (Schagen, 1974). Likewise, the SXI background noise contributions can range between 0.5 and 1.0 DN, depending upon circumstances. Hence we examine four separate models to bracket the likely behavior of the SXI system.

A simulation was developed to show the number of detected photons as a function of MCP gain voltage needed to achieve a SNR of 3.0, with the noisiest response being at the lower voltages. In addition, the SXI detector dynamic range was determined as a function of MCP gain voltage. (The dynamic range is defined as the ratio of the number of photons to full well versus the number of photons for SNR = 3.0.)

Four noise models are considered:

- Model A uses a constant $F_{\rm MCP} = 2.0$ suggested by the pulse height distribution. N_D and N_Q are both set to 0.5 DN.
- Model B uses the functional form $F_{\rm MCP} = 33.55 - 9.91671 \times \log_{10}(g)$, based upon Schagen (1974). N_D and N_Q are again both set to 0.5 DN.
- Model C is the same as Model A except N_D and N_Q are both set to 1.0 DN.
- Model D is the same as Model B except N_D and N_Q are both set to 1.0 DN.

Figure A1 depicts the results of the simulation.

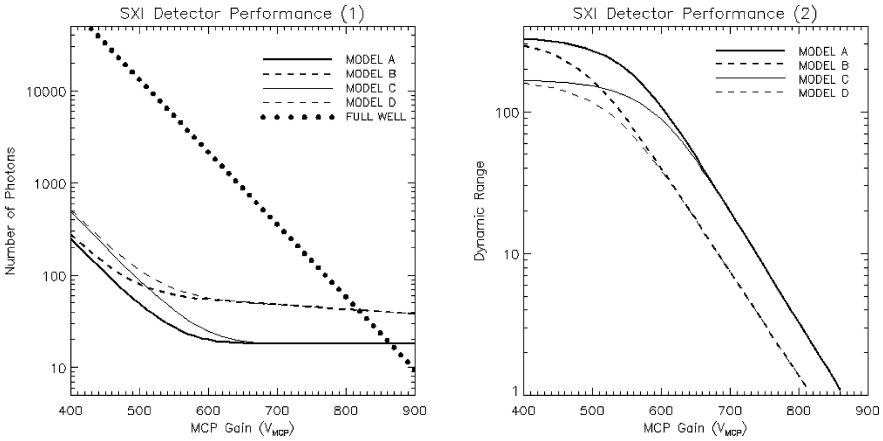

Figure A1. SXI performance as a function of MCP gain. The plot *at left* shows the number of photons needed to confirm detection (SNR = 3.0) for four different estimates of MCP and background noise levels (see text). The *dotted line* shows the number of photons needed to achieve full well in the CCD. The plot *at right* shows the detector dynamic range, defined as the ratio of photons for full well to photons for SNR = 3.0 detection.

References

Berthiaume, G. D.: 1998, GOES-M Solar X-ray Imager (SXI) Recalibration Report, pp. 63, Lincoln Laboratory, Lexington, Massachusetts.

Estrera, J. P., Ostromek, T. E., Bacarella, A. V., Isbell, W., Iosue, M. J., Saldana, M. R., and Beystrum, T. R.: 2003, 2002, *Proc. SPIE* **4796**, 49.

Gburek, S. and Sylwester, J.: 1999, In-flight analysis of the YOHKOH PSF function, in *Magnetic Fields and Solar Processes*, Proc. 9th European Meeting on Solar Physics, Florence, Italy, *ESA SP-448*, p. 819.

Guest, A. J.: 1971, *Acta Electronica* **14**, 107.

Hill, S. M., *et al.*: 2005, *Solar Phys.*, this issue.

Ientilucci, E. J.: 2000, Synthetic simulation and modeling of image intensified CCDs (IICCD), Master's Thesis, Rochester Institute of Technology, New York, p. 93.

Kuhn, J. R., Lin, H., and Loranz, D.: 1991, *Publ. Astronom. Soc. Pacific* **103**, 1097.

Martens, P. C., Acton, L. W., and Lemen, J. R.: 1995, *Solar Phys.* **157**, 141.

Mewe, R., Gronenschild, E. H. B. M., and Oord, G.H.J.v.d.: 1985, *Astron. Astrophys. Suppl. Series* **62**, 197.

O'Dell, S. L. et al.: 2000, *Proc. SPIE* **4140**, 99.

Russell, K., Briscoe, J., Corder, E., Wallace, S., and Chappell, J. H.: 1996, *Proc. SPIE* **2812**, 638.

Schagen, P.: 1974, in B. Kagan (ed.), *Advances in Image Pickup and Display*, **1**, Academic Press, New York, pp. 1.

Sturrock, P. A., Wheatland, M. A., and Acton, L. W.: 1996, *Astrophys. J. Lett.* **461**, L115.

Sudey, J.: 2002a, GOES-12 Dynamic Interactions PLT, Swales Aerospace.

Sudey, J.: 2002b, SADA stepping PLT, Swales Aerospace.

Vaiana, G. S., van Speybroeck, L., Zombeck, M. V., Krieger, A. S., Silk, J. K., and Timothy, A.: 1977, *Space. Sci. Inst.* **3**, 19.

VanSpeybroeck, L. P. and Chase, R. C.: 1972, *Applied Optics*, **11**, 440.

Zimmermann, F., Zwirn, G., and Davis, M. A.: 2004, *Proc. SPIE* **5171**, 326.